Nanoscale

PAPER

View Article Online
View Journal | View Issue

Cite this: *Nanoscale*, 2017, **9**, 1972

Bottom-up synthesis of nitrogen-doped porous carbon scaffolds for lithium and sodium storage†

Hongling Lu,‡[a] Renpeng Chen,‡[a] Yi Hu,[a] Xiaoqi Wang,[a] Yanrong Wang,[a] Lianbo Ma,[a] Guoyin Zhu,[a] Tao Chen,[a] Zuoxiu Tie,[a,b] Zhong Jin*[a] and Jie Liu*[a,c]

Received 22nd October 2016,
Accepted 13th January 2017

DOI: 10.1039/c6nr08296c

rsc.li/nanoscale

Here we report an effective bottom-up solution-phase process for the preparation of nitrogen-doped porous carbon scaffolds (NPCSs), which can be employed as high-performance anode materials for both lithium-ion batteries (LIBs) and sodium-ion batteries (SIBs). The as-obtained NPCSs show favorable features for electrochemical energy storage such as high specific surface area, appropriate pore size distribution (3.9 nm in average), large pore volume (1.36 cm^3 g^{-1}), nanosheet-like morphology, a certain degree of graphitization, enlarged interlayer distance (0.38 nm), high content of nitrogen (~5.6 at%) and abundant electrochemically-active sites. Such a unique architecture provides efficient Li^+/Na^+ reservoirs, and also possesses smooth electron transport pathways and electrolyte access. For LIBs, the anodes based on NPCSs deliver a high reversible capacity of 1275 mA h g^{-1} after 250 cycles at 0.5 C (1 C = 372 mA g^{-1}), and outstanding cycling stabilities with a capacity of 518 mA h g^{-1} after 500 cycles at 5 C and 310 mA h g^{-1} after 1500 cycles even at 10 C. For SIBs, the anodes based on NPCSs display a reversible capacity of 257 mA h g^{-1} at 50 mA g^{-1}, and superior long-term cycling performance with a capacity of 191 mA h g^{-1} after 1000 cycles at 200 mA g^{-1}.

Introduction

The increasing global demand of portable electronics and electric vehicles has greatly promoted research interest to develop rechargeable lithium ion batteries (LIBs) and other alternatives, such as sodium ion batteries (SIBs).[1,2] Graphite, the most commonly used commercial anode material for LIBs, suffers from several disadvantages, such as low theoretical specific capacity (372 mA h g^{-1}) and limited rate capability.[3] Furthermore, graphite can hardly be intercalated by Na^+ in SIBs due to its unfavorable structure and narrow interplanar spacing towards Na^+ insertion.[4,5] Therefore, it is of great importance to search for new anode materials with high energy density and good cyclability for both LIBs and SIBs. In the past decade, many carbonaceous materials, such as carbon nanotubes,[6] graphene[7] and mesoporous carbon,[8,9] have been investigated as anode materials for LIBs, exhibiting high performance of lithium storage owing to the good electronic conductivity and rapid ion transportation. For SIBs, diverse carbon materials have also been investigated as anode materials.[10–14] Generally, a good carbonaceous anode material for SIBs should consist of few-layer-stacked graphitic nanocrystallites and disordered structures with interlayer distances of ≥0.37 nm that can facilitate sodiation/desodiation. These carbon-based SIB anodes usually present a reversible capacity of about ~300 mA h g^{-1} at a low current density (below 50 mA g^{-1}). In the present circumstances, it is very important to further improve the specific capacity and rate performance of carbonaceous anode materials.

A promising strategy to enhance the energy storage performance of carbon-based materials is to introduce heteroatoms, such as N, P, S and B.[15–21] Due to the substitution of heteroatoms, the electrochemical activity and reversible capacity for Li^+ and Na^+ storage can be improved in varying degrees. In particular, nitrogen doping is very attractive among the heteroatom substitutions, because the interaction of a carbon matrix with lithium/sodium ions can be greatly enhanced by the strong electronegativity of nitrogen atoms.[15] Moreover, plenty of defects and vacancies can be introduced by nitrogen doping, thus the number of electroactive sites and the wettability to electrolytes would be significantly increased.[22,23] Nevertheless, if the nitrogen content is too high, the porosity and conductivity of the carbon matrix may be decreased. Therefore, it remains a challenge to design and

[a]*Key Laboratory of Mesoscopic Chemistry of MOE and Collaborative Innovation Center of Chemistry for Life Sciences, School of Chemistry and Chemical Engineering, Nanjing University, Nanjing, Jiangsu 210093, China. E-mail: zhongjin@nju.edu.cn, j.liu@duke.edu*

[b]*College of Engineering and Applied Sciences, Nanjing University, Nanjing, Jiangsu 210093, China*

[c]*Department of Chemistry, Duke University, Durham, North Carolina, 27708, USA*

†Electronic supplementary information (ESI) available. See DOI: 10.1039/c6nr08296c

‡These authors contributed equally to this work.

synthesize heteroatom-doped carbonaceous materials with optimized porosity and appropriate elemental doping configuration to further enhance the capacity of Li^+ and Na^+ storage.

Herein, we report a facile solution-phase bottom-up synthesis of nitrogen-doped porous carbon scaffolds (NPCSs) with high performances as anode materials in LIBs and SIBs. Benefiting from the unique architecture, the as-obtained NPCSs possess remarkable features of moderate nitrogen doping, appropriate surface area and pore size to facilitate electrolyte access and allow rapid charge transfer. Besides, the enlarged interlayer distance (0.38 nm) is favorable for the insertion/extraction of Na^+. Compared to the control sample of pristine carbon scaffolds (PCSs) without nitrogen doping, the resultant NPCSs were found to be a superior anode material with high reversible capacity, excellent rate capability and long-term cycling performance for both LIBs and SIBs.

Experimental

Chemicals

All chemicals in this work are of analytical purity and used without further purification.

Bottom-up solution-phase synthesis of NPCSs

Typically, 50 mL of paraffin oil was put into a 100 mL nitrogen-purged three-neck round-bottom flask equipped with a magnetic stir bar, a nitrogen gas inlet, a stopper, and an air reflux condenser connected to an oil bubbler. 1.2 mL of tetrachloroethylene was added into the paraffin oil as the carbon source. Subsequently, 1.84 g of cyanuric chloride (carbon and nitrogen source) and 2.6 g of sodium metal were slowly added into the mixture under a nitrogen gas flow. After all the reagents were added, the flask was heated to 350 °C under an N_2 atmosphere under refluxing and continuous stirring for 8 h. In this process, sodium metal reacted with tetrachloroethylene and cyanuric chloride to carry out dechlorination and carbonization, resulting in NPCSs and sodium chloride. After cooling down to room temperature, the resultant brown powder was filtered through a PTFE membrane (0.2 μm pores) and washed sequentially with 200 mL of petroleum ether, acetone, deionized water and ethanol to remove residual organic compounds and inorganic salts. After drying in a vacuum oven at 100 °C, the as-obtained dark powder was annealed at 900 °C for 1 h under an Ar atmosphere in a tube furnace with a ramp rate of 2 °C min^{-1} to obtain the final product.

Synthesis of pristine carbon scaffolds (PCSs)

For the preparation of PCSs, the experimental process similar to that of NPCSs was carried out, except that less sodium (1.3 g) and no cyanuric chloride were used.

Instrumentation and characterizations

The morphology of samples was characterized with a scanning electron microscope (SEM, Hitachi S-4800) coupled with an energy-dispersive X-ray spectrometer (EDX). Transmission electron microscopy (TEM) observation was carried out on a JEM-2100 instrument. Powder X-ray diffraction spectra (XRD) from 10° to 80° were recorded using an X-ray diffractometer (Bruker D-8 Advance, Cu Kα radiation at 40 kV and 40 mA) at a scanning rate of 6° min^{-1}. X-ray photoelectron spectra (XPS) were collected with a PHI-5000 VersaProbe X-ray photoelectron spectrometer with an Al Kα X-ray radiation. Raman spectra were collected with a Horiba JY H800 Raman spectrometer using a 532 nm laser source. Nitrogen adsorption–desorption isotherms were measured through Brunauer–Emmett–Teller (BET) analysis on a Quantachrome Autosorb-IQ-2Canalyzer at liquid-nitrogen temperature. The elemental analysis was carried out on an elemental analyzer (CHN-O-Rapid). The FT-IR spectrum was recorded on a Fourier transform infrared spectrometer (NEXUS870).

Electrochemical measurements

The electrochemical performances of the samples were measured in the form of 2032 coin-type cells. The LIBs and NIBs were assembled in an argon-filled glovebox (with the content of O_2 and H_2O less than 0.1 ppm). For LIB tests, Li metal foil was used as a counter electrode, a solution of $LiPF_6$ (1.0 mol L^{-1}) in a mixture of ethylene carbonate, diethyl carbonate and dimethyl carbonate (1 : 1 : 1 by volume) was used as an electrolyte, and a Celgard-2400 membrane was used as a separator. For SIB tests, Na metal was used as a counter electrode, a solution of $NaClO_4$ (1.0 mol L^{-1}) in a mixture of ethylene carbonate and propylene carbonate (2 : 1 by volume) was used as an electrolyte, and glass fiber membrane (GF/D, Whatman) was used as a separator. For the preparation of anodes, a slurry containing active materials (NPCSs or PCSs, 80 wt%), super P (10 wt%) and PVDF (10 wt%) was uniformly mixed by using NMP and coated onto a copper foil substrate, and then dried in a vacuum oven at 100 °C for 12 h before testing. The loading mass of the active material is ~1.0 mg cm^{-2}. The galvanostatic discharge/charge tests were carried out between 0.01 and 3.0 V *vs.* Li^+/Li or Na^+/Na on a LAND CT2001A multichannel battery test system. Cyclic voltammetry (CV) and electrochemical impedance spectroscopy (EIS) measurements were performed with a CHI 760E electrochemical workstation (Shanghai Chenhua, China). CV was measured at a voltage range between 0.01 and 3.0 V *vs.* Li^+/Li or Na^+/Na with a scan rate of 0.2 mV s^{-1}. EIS was measured in the frequency range of 100 kHz–10 mHz with a disturbance amplitude of 5 mV.

Results and discussion

Characterization

The analytical evidences indicated that the carbon nanosheets were produced and assembled by the solution-phase reaction. Based on the feedstocks and experimental conditions, it could be deduced that a Wurtz reaction had occurred in the reactor. During this reaction process, dechlorination and carbonization

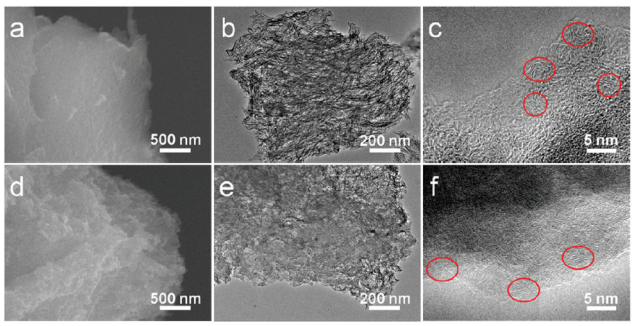

Fig. 1 (a) SEM image, (b) TEM image and (c) HRTEM image of NPCSs. (d) SEM image, (e) TEM image and (f) HRTEM image of PCSs as a control sample without nitrogen-doping.

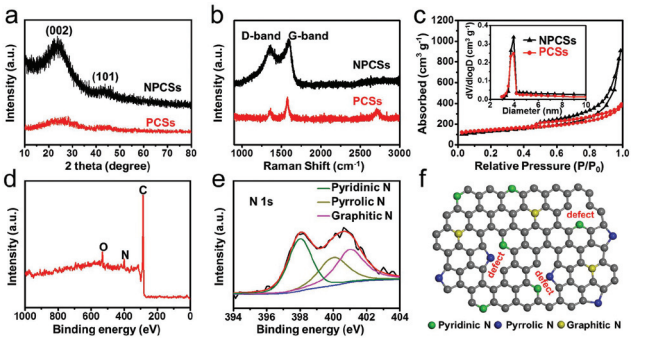

Fig. 2 (a) XRD patterns, (b) Raman spectra and (c) nitrogen adsorption–desorption isotherms of NPCSs and PCSs. The inset of (c) shows the pore size distributions of these two samples. (d) XPS survey spectrum, (e) high-resolution XPS spectrum in the N 1s region and (f) schematic structure of NPCSs.

were carried out by the reaction between sodium and tetrachloroethylene/cyanuric chloride. After further carbonization and purification, residual organic compounds and inorganic salts were removed and thus NPCSs were obtained. Moreover, abundant mesopores were formed by the removal of inorganic salts and the stacking of nitrogen-doped graphene-like carbon sheets. As shown in the SEM and TEM images (Fig. 1), both the as-obtained NPCSs and PCSs (control sample without nitrogen-doping) show a nanosheet-like morphology with a few stacked carbon layers. The microstructures of NPCSs and PCSs were investigated by high-resolution TEM (HRTEM). As shown in Fig. 1c, the graphitic nanocrystallites of NPCSs and an average interlayer distance of 0.38 nm at the edge of carbon nanosheets were observed. While for PCSs, the observed interplanar distance is about 0.35 nm (Fig. 1f). Such results reveal that the introduction of N atoms is effective in enlarging the interlayer spacing of carbon scaffolds,[24,25] which is favorable for the insertion of Na^+. The stacked nanosheet architecture can offer shorter diffusion pathways for ion transport and decrease the diffusion resistance between the electrode and electrolyte. These advantages are beneficial to the electrochemical performance of anodes based on NPCSs.

Further structural characterization of the samples has been performed. The difference in the interlayer distance between NPCSs and PCSs was confirmed by XRD patterns. As shown in Fig. 2a, two broad peaks of (002) and (101) diffractions were presented. The (002) peaks of NPCSs and PCSs are centered at around 23.4° and 25.2°, respectively. The interlayer distances were calculated to be 3.79 Å for NPCSs and 3.53 Å for PCSs, well consistent with the HRTEM observations.

The graphitization degree of products was determined by Raman spectroscopy. For NPCSs (Fig. 2b), the D band (associated with defects) and G band (related to graphitic carbon) are centered at 1356 and 1591 cm^{-1}, respectively; while PCSs present a D band at 1356 cm^{-1} and a G band at 1574 cm^{-1}. The calculated intensity ratio of D and G bands (I_D/I_G) for NPCSs and PCSs is 0.83 and 0.71, respectively, indicating that PCSs possess a higher graphitized degree than NPCSs, meanwhile suggesting the higher content of defects in NPCSs. The 2D band of PCSs is located at 2709 cm^{-1} with an I_{2D}/I_G ratio of 0.85; however, the 2D band of NPCSs (~2710 cm^{-1}) is very weak, suggesting the lower graphitization degree. The FT-IR spectrum of NPCSs (Fig. S1†) shows two peaks located at 1576 cm^{-1} and 1242 cm^{-1}, corresponding to the C=N and C–N bonds, respectively, further confirming that the N heteroatoms were successfully doped in NPCSs.

To compare the pore structure of NPCSs and PCSs, nitrogen adsorption–desorption isotherms were measured. As shown in Fig. 2c, the Brunauer–Emmett–Teller (BET) specific surface areas of NPCSs and PCSs were calculated to be 435 and 510 $m^2\ g^{-1}$, respectively. The high surface area can offer abundant active interfaces for ion and charge transport, thus benefiting the electrochemical performance. The isotherms of both NPCSs and PCSs were classified as type IV isotherms with a clear hysteresis loop, indicating the existence of mesopores. This was further confirmed by the pore size distribution analysis (the inset in Fig. 2c) based on the Barrett–Joyner–Halenda (BJH) method, revealing that the average pore size is ~3.9 nm for NPCSs and ~3.8 nm for PCSs. The total pore volume of NPCSs and PCSs is 1.36 and 0.47 $cm^3\ g^{-1}$, respectively. The appropriate pore size and large pore volume are beneficial to rapid ion diffusion and electrochemical performance.

XPS measurements were performed to investigate the elemental compositions and valence states of NPCSs. As shown in Fig. 2d, C 1s, N 1s and O 1s peaks can be seen in the XPS survey spectrum. The atomic content of N in NPCSs measured by XPS is 5.7 at%, comparable to the nitrogen content measured by elemental analysis (5.6 at% or 6.3 wt%). The high-resolution N 1s spectrum of NPCSs (Fig. 2e) can be deconvoluted into three peaks, pyridinic N (398.2 eV), pyrrolic N (400.1 eV) and graphitic N (401.0 eV). Based on the XPS analysis, a possible structure illustration of NPCSs is given in Fig. 2f. The plentiful N-containing species can provide more active sites for Li^+/Na^+ adsorption as well as enhance the capacitive properties of NPCSs.[7,9,14,22,26] Due to their unique structural features, an appropriate degree of nitrogen-doping and graphitization, relative high specific surface area and abundant mesopores for rapid ion diffusion and adsorption,

the NPCSs were expected as a promising anode material for LIBs and SIBs.

Performance of NPCSs as anode materials for LIBs

The Li-ion storage properties of NPCSs and PCSs were evaluated using the standard half-cell configuration. CV profiles were recorded in the first four cycles in avoltage range of 0.01–3.0 V (*vs.* Li^+/Li). As shown in Fig. 3a, the rectangular shape at high potential is similar to the reported nitrogen-doped graphene with the combined pore storage mechanism and surface adsorption mechanism, owing to the high surface area and nitrogen doping.[15,25] Furthermore, the presence of the reduction peak at ~0.4 V in the first discharge step corresponds to the electrolyte decomposition and the formation of the solid electrolyte interphase (SEI) layer. In the following cycles, the intensity of this peak decreased significantly, indicating the occurrence of some side reactions and the loss of some lithium storage sites within the carbon scaffolds.[26] The CV curves of NPCSs are almost overlapped in the subsequent cycles, suggesting high stability and good reversibility. The peak at ~1.5 V belongs to the slightly oxidized surface layer formed on copper foil during storage. In the following scans, this peak disappeared due to the formation of an SEI film.[15,26] The CV curves of PCSs are shown in Fig. 3b, exhibiting electrochemical behavior similar to NPCSs.

The galvanostatic discharge/charge profiles of NPCSs in a potential window of 0.01–3.0 V (*vs.* Li^+/Li) during the first, second and tenth cycles at 0.1 C (1 C = 372 mA g^{-1}) are shown in Fig. 3c. It is observed that the potential plateaus are not prominent, suggesting the presence of multiple lithium storage mechanisms in NPCSs. Surprisingly, a very high initial discharge capacity of 2046 mA h g^{-1} is obtained, while the initial reversible capacity is 995 mA h g^{-1}, close to 3 times as compared to the theoretical capacity of graphite (372 mA h g^{-1}), which is attributed to the combined adsorption mechanism of lithium storage according to the literature.[27,29,30] The large irreversible capacity in the first cycle is 1051 mA h g^{-1}, which is ascribed to the decomposition of the electrolyte and the formation of the SEI layer on the surface of the electrode.[13–33] After the first cycle, the specific capacity becomes stable and highly reversible. The initial Coulombic efficiency of NPCSs is 48.6% at a current density of 37.2 mA g^{-1}, which is comparable to the previous reports.[9,26,34] The Coulombic efficiency increases dramatically with the increase of cycle numbers, reaching over 87% in the second cycle and over 94% in the tenth cycle.

In order to further evaluate the cycling performance, the anodes based on NPCSs and PCSs were tested at 0.5 C, as shown in Fig. 3d. After 250 cycles, the NPCS electrode still delivers a reversible capacity of 1275 mA h g^{-1} and the Coulombic efficiency is higher than 96%. Notably, although the capacity of NPCSs decreases in the first 20 cycles, it gradually increases again upon cycling after that. The increase of capacity may be attributed to the activation process of NPCSs with the electrolyte. In the initial several cycles, a large amount of Li^+ was embedded into the carbon layers of NPCSs or adsorbed by the nanopores, which may block the further Li^+ transmission from the electrode to the electrolyte, thus resulting in the decrease of capacity. During the following cycles, the interlayer spacing of carbon sheets becomes more expanded, which is favorable for the deintercalation of Li^+ from NPCSs. Meanwhile, the unique architecture of NPCSs can effectively shorten the diffusion length of ions, simultaneously increase the contact area and wettability between the electrode and the electrolyte, resulting in the increase of capacity after 20 cycles. Compared with NPCSs, PCSs exhibit similar lithium storage behavior but with much lower capacity. When tested at 0.5 C, the electrode based on PCSs only delivers a capacity of 438 mA h g^{-1}. We also investigated the influence of carbonization temperature on the performance of NPCSs. As presented in Fig. S2,† the NPCSs annealed at 800 °C and 1000 °C exhibit reversible capacities of 941 and 671 mA h g^{-1} after 250 cycles with a rate of 0.5 C, respectively. Therefore, the sample obtained at 900 °C shows the best lithium storage performance in this work.

Fig. 3e shows the rate capability of anodes based on NPCSs and PCSs at various current densities. At the current densities of 0.2 C, 0.5 C, 1 C and 2 C, the electrode based on NPCSs can reach reversible capacities of 849, 776, 629 and 540 mA h g^{-1}, whereas the PCS based electrode delivers low capacities of 249, 240, 228 and 192 mA h g^{-1}, respectively. Even at a high rate of 5 C, the electrode based on NPCSs can still reach a high capacity of 413 mA h g^{-1}. In comparison, the electrode based on PCSs can only deliver a low capacity of 142 mA h g^{-1} at 5 C. After being cycled at different rates, when the current density is reset to the initial value (0.2 C), the specific capacity of the NPCS-based electrode recovers to 895 mA h g^{-1}. Notably, when cycled at the high rates of 2 C and 5 C, the electrode based on NPCSs exhibited incredibly stable cycling stability, indicating that NPCSs possess excellent reversibility and highly stable cycling performance. Fig. 3f shows the Nyquist plots of the half-cell based on NPCSs before and after 250 cycles at the rate of 0.5 C, indicating that the impedance of NPCSs decreases upon long-term cycling after activation. The Nyquist plots of the half-cell based on PCSs before and after 250 cycles at 0.5 C are presented in Fig. S3.† The internal resistance of

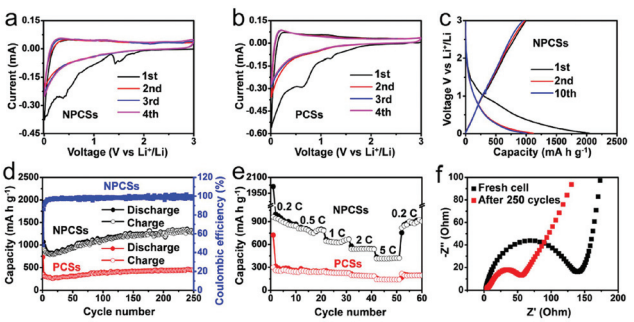

Fig. 3 Electrochemical performances of NPCSs and PCSs as anode materials for LIBs: CV curves of (a) NPCSs and (b) PCSs at a sweep rate of 0.2 mV s^{-1}. (c) Discharge/charge curves of NPCSs at 0.1 C. (d) Cyclability and Coulombic efficiency of NPCSs and PCSs at 0.5 C. (e) Rate performance of NPCSs and PCSs at different current densities. (f) Nyquist plots of the half-cell based on NPCSs before and after 250 cycles at 0.5 C.

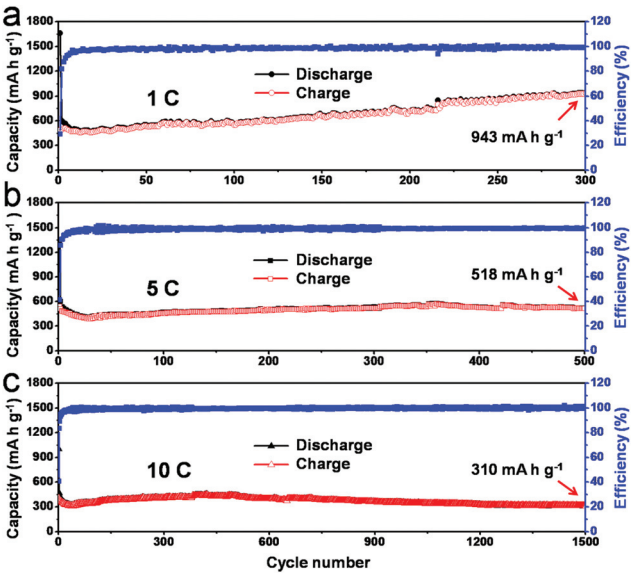

Fig. 4 Cycling performance of NPCS-based anodes for LIBs at (a) 1 C, (b) 5 C and (c) 10 C, respectively.

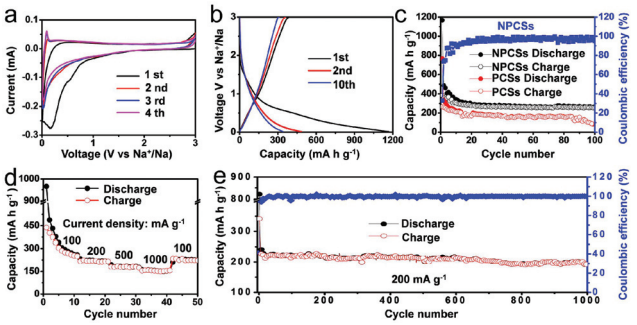

Fig. 5 Electrochemical performances of NPCSs and PCSs as anode materials for SIBs: (a) CV curves of NPCSs at a sweep rate of 0.2 mV s^{-1}. (b) Discharge/charge curves of NPCSs at a current density of 50 mA g^{-1}. (c) Cycling performances of anodes based on NPCSs and PCSs at a current density of 50 mA g^{-1}. (d) Rate performance of NPCSs. (e) Long-term cyclability and Coulombic efficiency of NPCSs at 200 mA g^{-1}.

the half-cell based on NPCSs is lower than that of PCSs, suggesting that the N heteroatoms are beneficial to the conductivity of carbon scaffolds in this work.

The long-term cycling performance of NPCSs for LIBs was also evaluated at different current densities (Fig. 4). The NPCS-based anodes exhibit high reversible capacities of 943, 518, and 310 mA h g^{-1} after 300, 500, and 1500 cycles with a rate of 1 C, 5 C and 10 C, respectively.

Performance of NPCSs as anode materials for SIBs

Different from lithium storage, the sodium storage performances of carbon scaffolds are greatly influenced by the interlayer distance. As mentioned above, the interlayer distance of NPCSs was enlarged to 3.8 Å by the introduction of nitrogen heteroatoms. Besides, more defects and electrochemical active sites were formed by nitrogen doping, which can accommodate more Na^+ and also facilitate Na^+ insertion/extraction.[19,20,28]

The electrochemical performances of NPCSs and PCSs as anode materials for SIBs were evaluated by galvanostatic discharge/charge processes, as shown in Fig. 5. Fig. 5a shows the CV curves of the NPCS-based electrode. In the first cycle, the peak at 0.6 V could be attributed to the formation of a SEI film.[28,35] The CV curves mostly overlapped in the following cycles, indicating the formation of a stable SEI film and the good reversibility of electrochemical reactions. Fig. 5b shows the discharge/charge profiles of NPCSs for the first, second and tenth cycles at a current density of 50 mA g^{-1}. In the first cycle, the electrode exhibits a large initial discharge capacity of 1167 mA h g^{-1}. The obscure plateau centered at about 0.6 V is ascribed to the formation of the SEI film, in accordance with the CV results. The plateau region at low voltage (<0.2 V) indicates that a portion of capacity originated from the Na^+ adsorption by nanopores.[19] As the cycling progresses, a stable SEI film is formed, resulting in a stable capability. The cycling performance of NPCSs and PCSs at a current density of 50 mA g^{-1} is presented in Fig. 5c. The electrode based on NPCSs maintains a high reversible capacity of 268 mA h g^{-1} after 100 cycles. The capacity retention measured from the tenth cycle is about 82%. In contrast, the PCS-based anode only delivers a low capacity of 89 mA h g^{-1} after 100 cycles.

The rate capability of the NPCS-based electrode at various current densities is shown in Fig. 5d. At the current densities of 100, 200, 500 and 1000 mA g^{-1}, the reversible capacities were measured to be 260, 220, 180 and 155 mA h g^{-1}, respectively. When the current density was reduced to 100 mA g^{-1}, the specific capacity recovered to 225 mA h g^{-1}, indicating the good rate performance of NPCSs.

The long-term cycling performance of the NPCS-based electrode for SIBs was evaluated at a current density of 200 mA g^{-1}. As shown in Fig. 5e, the reversible capacity can reach 341 mA h g^{-1} in the first cycle. Even after 1000 cycles, the capacity still maintains at 191 mA h g^{-1} with a Coulombic efficiency over 99%, confirming the high stability of the NPCS-based electrode upon Na^+ intercalation/deintercalation.

Conclusions

According to the characterization and electrochemical tests, the good lithium and sodium storage performances of NPCSs are attributed to the following factors: (1) the unique nanostructure with a high surface area, appropriate pore size and large pore volume can serve as high-capacity reservoirs for Li^+/Na^+, and also provide a large electrode/electrolyte contact area and short diffusion distance; (2) the introduction of nitrogen heteroatoms can enlarge the interlayer distance (~3.8 Å) and create more electrochemically active sites, which can accommodate more Li^+/Na^+ and also facilitate the insertion and extraction of Li^+/Na^+. Considering the outstanding electrochemical performances and facial synthesis approach, NPCSs

are suggested to be a promising anode material for both LIBs and SIBs, and may also be used for other applications of energy storage and conversion.

Acknowledgements

This work was supported by the National Materials Genome Project (2016YFB0700600), the National 973 Basic Research Program (2015CB659300), the National Natural Science Foundation of China (21403105, 21573108), the China Postdoctoral Science Foundation (2015M580413, 2015M581769), the Natural Science Foundation for Young Scholars of Jiangsu Province (BK20150583, BK20160647), the Fundamental Research Funds for the Central Universities and a project funded by the Priority Academic Program Development (PAPD) of Jiangsu Higher Education Institutions.

Notes and references

1 J. M. Tarascon and M. Armand, *Nature*, 2001, **414**, 359–367.
2 S. W. Kim, D. H. Seo, X. Ma, G. Ceder and K. Kang, *Adv. Energy Mater.*, 2012, **2**, 710–721.
3 N. A. Kaskhedikar and J. Maier, *Adv. Mater.*, 2009, **21**, 2664–2680.
4 D. A. Stevens and J. R. Dahn, *J. Electrochem. Soc.*, 2001, **148**, 803–811.
5 Y. R. Wang, R. P. Chen, T. Chen, H. L. Lv, G. Y. Zhu, L. B. Ma, C. X. Wang, Z. Jin and J. Liu, *Energy Storage Mater.*, 2016, **4**, 103–129.
6 B. J. Landi, M. J. Ganter, C. D. Cress, R. A. DiLeo and R. P. Raffaelle, *Energy Environ. Sci.*, 2009, **2**, 638–654.
7 Z. S. Wu, W. Ren, L. Xu, F. Li and H. M. Cheng, *ACS Nano*, 2011, **5**, 5463–5471.
8 K. T. Lee, J. C. Lytle, N. S. Ergang, S. M. Oh and A. Stein, *Adv. Funct. Mater.*, 2005, **15**, 547–556.
9 F. C. Zheng, Y. Yang and Q. W. Chen, *Nat. Commun.*, 2014, **5**, 5261.
10 D. A. Stevens and J. R. Dahn, *J. Electrochem. Soc.*, 2000, **147**, 1271–1273.
11 K. Tang, L. Fu, R. J. White, L. Yu, M. M. Titirici, M. Antonietti and J. Maier, *Adv. Energy Mater.*, 2012, **2**, 873–877.
12 Y. L. Cao, L. Xiao, M. L. Sushko, W. Wang, B. Schwenzer, J. Xiao, Z. M. Nie, L. V. Saraf, Z. G. Yang and J. Liu, *Nano Lett.*, 2012, **12**, 3783–3787.
13 Y. X. Wang, S. L. Chou, H. K. Liu and S. X. Dou, *Carbon*, 2013, **57**, 202–208.
14 S. Li, J. X. Qiu, C. Lai, M. Ling, H. J. Zhao and S. Q. Zhang, *Nano Energy*, 2015, **12**, 224–230.
15 Y. Mao, H. Duan, B. Xu, L. Zhang, Y. S. Hu, C. C. Zhao, Z. X. Wang, L. Q. Chen and Y. S. Yang, *Energy Environ. Sci.*, 2012, **5**, 7950–7955.
16 C. Z. Zhang, N. Mahmood, H. Yin, F. Liu and Y. L. Hou, *Adv. Mater.*, 2013, **25**, 4932–4937.
17 S. Y. Yuan, J. W. L. Bao, L. N. Wang, Y. Y. Xia, D. G. Truhlar and Y. G. Wang, *Adv. Energy Mater.*, 2016, **6**, 1501733.
18 J. H. Hou, C. B. Cao, F. Idrees and X. L. Ma, *ACS Nano*, 2015, **9**, 2556–2564.
19 L. Qie, W. M. Chen, X. Q. Xiong, C. C. Hu, F. Zou, P. Hu and Y. H. Huang, *Adv. Sci.*, 2015, **2**, 1500195.
20 D. F. Xu, C. J. Chen, J. Xie, B. Zhang, L. Miao, J. Cai, Y. H. Huang and L. N. Zhang, *Adv. Energy Mater.*, 2016, **6**, 1501929.
21 Z. Jin, Z. Z. Sun, L. J. Simpson, K. J. O'Neill, P. A. Parilla, Y. Li, N. P. Stadie, C. C. A. Ahn, C. Kittrell and J. M. Tour, *J. Am. Chem. Soc.*, 2010, **132**, 15246–15251.
22 H. Wang, C. Zhang, Z. Liu, L. Wang, P. Han, H. Xu, K. Zhang, S. Dong, J. Yao and G. Cui, *J. Mater. Chem.*, 2011, **21**, 5430–5434.
23 J. Zhao, H. Lai, Z. Lyu, Y. Jiang, K. Xie, X. Wang, Q. Wu, L. Yang, Z. Jin, Y. Ma, J. Liuand and Z. Hu, *Adv. Mater.*, 2016, **27**, 3541–3545.
24 L. Qu, Y. Liu, J.-B. Baek and L. Dai, *ACS Nano*, 2010, **4**, 1321–1326.
25 X. Teng, C. Ma, C. Ge, M. Yan, J. Yang, Y. Zhang, P. C. Morais and H. Bi, *J. Mater. Chem. B*, 2014, **2**, 4631–4639.
26 W. Ai, Z. M. Luo, J. Jiang, J. H. Zhu, Z. Z. Du, Z. X. Fan, L. H. Xie, H. Zhang, W. Huang and T. Yu, *Adv. Mater.*, 2014, **26**, 6186–6192.
27 J. N. Gu, Z. G. Du, C. Zhang and S. B. Yang, *Adv. Energy Mater.*, 2016, **6**, 1600917.
28 D. D. Li, L. Zhang, H. B. Chen, L. X. Ding, S. Q. Wang and H. H. Wang, *Chem. Commun.*, 2015, **51**, 16045–16048.
29 Z. L. Wang, D. Xu, H. G. Wang, Z. Wu and X. B. Zhang, *ACS Nano*, 2013, **7**, 2422–2430.
30 S. B. Yang, X. L. Feng, L. J. Zhi, Q. Cao, J. Maier and K. Mullen, *Adv. Mater.*, 2010, **22**, 838–842.
31 W. H. Shin, H. M. Jeong, B. G. Kim, J. K. Kang and J. W. Choi, *Nano Lett.*, 2012, **12**, 2283–2288.
32 J. R. Dahn, T. Zheng, Y. H. Liu and J. S. Xue, *Science*, 1995, **270**, 590–593.
33 B. K. Guo, X. Q. Wang, P. F. Fulvio, M. F. Chi, S. M. Mahurin, X. G. Sun and S. Dai, *Adv. Mater.*, 2011, **23**, 4661–4666.
34 Y. Fang, Y. Y. Lv, R. C. Che, H. Y. Wu, X. H. Zhang, D. Gu, G. F. Zheng and D. Y. Zhao, *J. Am. Chem. Soc.*, 2013, **135**, 1524–1530.
35 W. Ai, L. H. Xie, Z. Z. Du, Z. Y. Zeng, J. Q. Liu, H. Zhang, Y. H. Huang and T. Yu, *Sci. Rep.*, 2013, **3**, 2341.